

Diffusion in arrays of obstacles: beyond homogenisation

Yahya Farah¹, Daniel Loghin¹, Alexandra Tzella^{1*} and Jacques Vanneste²

¹School of Mathematics, University of Birmingham, Birmingham, UK,

² School of Mathematics and Maxwell Institute for Mathematical Sciences,
University of Edinburgh, Edinburgh, UK

December 21, 2024

Abstract

We revisit the classical problem of diffusion of a scalar (or heat) released in a two-dimensional medium with an embedded periodic array of impermeable obstacles such as perforations. Homogenisation theory provides a coarse-grained description of the scalar at large times and predicts that it diffuses with a certain effective diffusivity, so the concentration is approximately Gaussian. We improve on this by developing a large-deviation approximation which also captures the non-Gaussian tails of the concentration through a rate function obtained by solving a family of eigenvalue problems. We focus on cylindrical obstacles and on the dense limit, when the obstacles occupy a large area fraction and non-Gaussianity is most marked. We derive an asymptotic approximation for the rate function in this limit, valid uniformly over a wide range of distances. We use finite-element implementations to solve the eigenvalue problems yielding the rate function for arbitrary obstacle area fractions and an elliptic boundary-value problem arising in the asymptotics calculation. Comparison between numerical results and asymptotic predictions confirm the validity of the latter.

1 Introduction

We consider the diffusion of a passive scalar inside a two-dimensional homogeneous medium interrupted by an infinite number of impermeable obstacles (e.g., perforations) arranged in a periodic lattice, as illustrated in Fig. 1 for the case of circular obstacles. The scalar concentration $\theta(\mathbf{x}, t)$ satisfies the dimensionless diffusion equation

$$\frac{\partial \theta}{\partial t} = \nabla^2 \theta, \tag{1a}$$

*Corresponding author: a.tzella@bham.ac.uk

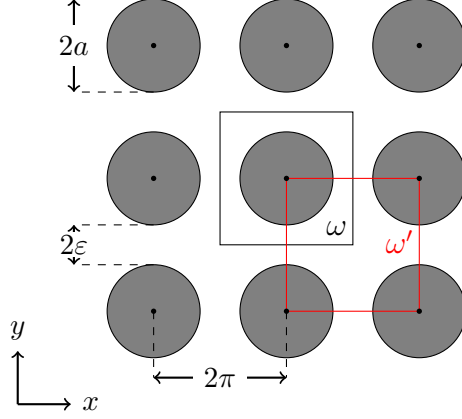


Figure 1: Square lattice of circular obstacles indicating the problem’s geometric parameters and the two alternative elementary cells ω and ω' used in the analysis.

with no-flux conditions on the boundaries \mathcal{B} of the obstacles,

$$\mathbf{n} \cdot \nabla \theta = 0 \quad \text{on } \mathcal{B}, \quad (1b)$$

where \mathbf{n} denotes the outward normal to \mathcal{B} . The concentration is a function of the dimensionless position vector $\mathbf{x} = (x, y)^T$ scaled by a reference length scale ℓ related to the lattice period, and time t scaled by the diffusive timescale ℓ^2/κ , where κ is the molecular diffusivity.

We are interested in the initial-value problem corresponding to the instantaneous release of the scalar at some location \mathbf{x}_0 outside the obstacles. Our aim is to provide a coarse-grained description of $\theta(\mathbf{x}, t)$, valid when the scalar has spread over many periods of the lattice. This problem and its steady-state counterpart have a long history, dating back to Maxwell [14] and Rayleigh [17], driven by their relevance to a broad range of applications that include constituent dispersion, heat conduction (with θ the temperature) and (with suitable re-interpretation) electric conduction and electrostatics, in porous media and in composite materials (see e.g. Ch. 2 of [6] for a survey). The central conclusion is that coarse-graining results in a diffusion equation,

$$\frac{\partial \theta}{\partial t} = \kappa_{\text{eff}} \nabla^2 \theta, \quad (2)$$

for the large-scale concentration, with an *effective diffusivity* κ_{eff} that accounts for the effect of the obstacles. Note that this effect results from two competing mechanisms: obstacles reduce the area available to the scalar, which enhances dispersion, but they also reduce the scalar flux, which inhibits dispersion. The second mechanism is dominant so that $\kappa_{\text{eff}} \leq 1$ (see e.g. Ch. 1 of [12]).

Homogenisation theory [e.g. 11, 19] provides a set of techniques for the computation of κ_{eff} that extends and systematises the approaches used by the early pioneers. Explicit asymptotic results, valid when the obstacles occupy a small or large area fraction σ , are particularly valuable. For small area fraction – the dilute limit – Maxwell and Rayleigh’s results [14, 17] yield

$$\kappa_{\text{eff}} \sim 1 - \sigma \quad \text{as } \sigma \rightarrow 0, \quad (3)$$

while for near-maximal area fractions – the dense limit – and for circular obstacles in the configuration of Fig. 1 Keller [13] obtains

$$\kappa_{\text{eff}} \sim \frac{2(\pi/4 - \sigma)^{1/2}}{\pi^{3/2}(1 - \pi/4)} \quad \text{as } \sigma \rightarrow \pi/4. \quad (4)$$

Between these two limits, the value of κ_{eff} can be computed numerically [16].

The present paper is motivated by the recognition that, for the initial-value problem, the diffusion approximation (2) predicted by homogenisation has limitations, specifically that it applies only to the core of the scalar distribution, $|\mathbf{x} - \mathbf{x}_0| = O(\sqrt{t})$, and fails in the tails, $|\mathbf{x} - \mathbf{x}_0| \gg \sqrt{t}$. This is particularly significant for applications in which low concentrations are critical, such as the migration of radioactive elements from underground nuclear water repositories which has been examined using homogenisation [2, 3]. Our aim, therefore, is to develop a coarse graining of (1) that goes beyond homogenisation and captures the tails of the scalar distribution. This can be achieved by applying ideas of large-deviation theory [e.g. 20], adapting the approach developed by [10] for transport in periodic fluid flow to the diffusion with obstacles (1). The approach, which we introduce in §2, provides an approximation to the concentration $\theta(\mathbf{x}, t)$ that is valid for $|\mathbf{x} - \mathbf{x}_0| = O(t)$, thus improving on homogenisation; it requires the solution of a family of eigenvalue problems which can be regarded as a generalisation of the cell problem of homogenisation. These eigenvalue problems also determine the speed of propagation of certain reaction fronts [5] so our results are also useful in this context.

In §§3–4, we focus on circular obstacles in the geometry of Fig. 1 and obtain explicit results demonstrating the value of the large-deviation approach. We first solve the family of eigenvalue problems numerically for different obstacle area fractions σ (§3). The results show that diffusion with κ_{eff} provide a satisfactory approximation of the concentration tails only in the dilute limit $\sigma \rightarrow 0$; for general σ and, most markedly in the dense limit $\sigma \rightarrow \pi/4$, the tails are much fatter than predicted by the diffusive approximation and display some anisotropy. To explore this further, we examine the dense limit in detail in §4, where we develop an asymptotic theory which extends Keller’s result (4) to the large-deviation regime. This theory, based on a matched-asymptotics treatment of the large-deviation eigenvalue problems, recovers and subsumes a more straightforward extension, which replaces the continuous geometry by that of a network [6] and captures part of the concentration tails. We assess the ranges of validity of the various approximations and test them against numerical solutions of the eigenvalue problems.

2 Large-deviation approximation

Our goal is to obtain an approximation for the concentration $\theta(\mathbf{x}, t)$ for long times $t \gg 1$. The theory of large deviations [9, 8, 20] applied to periodic environments indicates that it takes the two-scale form [10, 22]

$$\theta(\mathbf{x}, t) = \phi(\mathbf{x}, \boldsymbol{\xi}, t) e^{-tg(\boldsymbol{\xi})}, \quad \text{where } \boldsymbol{\xi} = \frac{\mathbf{x} - \mathbf{x}_0}{t} \in \mathbb{R}^2 \quad (5)$$

and \mathbf{x}_0 is the location of the initial scalar release, such that $\theta(\mathbf{x}, 0) = \delta(\mathbf{x} - \mathbf{x}_0)$. Here g is a rate (or Cramér) function which provides a continuous approximation for the most rapid changes in θ . It is non-negative, convex, and has a single minimum and zero located at $\boldsymbol{\xi} = \mathbf{0}$ that yields the maximum of θ in the limit of $t \rightarrow \infty$. The (positive) correction term ϕ (with $\ln \phi = o(t)$ as $t \rightarrow \infty$) has the same periodicity as the lattice,

$$\phi(\mathbf{x} + \mathbf{r}_{m,n}, \boldsymbol{\xi}, t) = \phi(\mathbf{x}, \boldsymbol{\xi}, t), \quad (6)$$

where $\mathbf{r}_{m,n}$ with $(m, n) \in \mathbb{Z}^2$ denotes the positions of the centroids of the obstacles.

Eq. (5) introduces the vector $\boldsymbol{\xi} = (\xi, \eta)^T$ defined on the whole of \mathbb{R}^2 which captures variations on scales large compared with the size of the lattice cells. The vector \mathbf{x} , in contrast, is defined on the multiply-connected domain obtained by excising the obstacles from \mathbb{R}^2 and captures variations on the scale of single lattice cells. The large separation between the two scales allows \mathbf{x} and $\boldsymbol{\xi}$ to be treated as independent. Introducing (5) into (1a) then gives

$$\begin{aligned} & (\nabla^2 - 2\nabla_{\boldsymbol{\xi}} g \cdot \nabla + |\nabla_{\boldsymbol{\xi}} g|^2 - \boldsymbol{\xi} \cdot \nabla_{\boldsymbol{\xi}} g + g - \partial_t) \phi \\ & + t^{-1} ((\boldsymbol{\xi} + 2\nabla - 2\nabla_{\boldsymbol{\xi}} g) \cdot \nabla_{\boldsymbol{\xi}} - \nabla_{\boldsymbol{\xi}}^2 g) \phi + t^{-2} \nabla_{\boldsymbol{\xi}}^2 \phi = 0 \end{aligned} \quad (7a)$$

while the boundary conditions (1b) become

$$\mathbf{n} \cdot (\nabla - \nabla_{\boldsymbol{\xi}} g + t^{-1} \nabla_{\boldsymbol{\xi}}) \phi = 0 \quad \text{on } \mathcal{B}. \quad (7b)$$

Substituting the expansion

$$\phi(\mathbf{x}, \boldsymbol{\xi}, t) = t^{-1} (\phi_0(\mathbf{x}, \boldsymbol{\xi}) + t^{-1} \phi_1(\mathbf{x}, \boldsymbol{\xi}) + t^{-2} \phi_2(\mathbf{x}, \boldsymbol{\xi}) + \dots), \quad (8)$$

with the prefactor t^{-1} motivated by mass conservation [10], into (7) gives

$$\nabla^2 \phi_0 - 2\mathbf{p} \cdot \nabla \phi_0 + |\mathbf{p}|^2 \phi_0 = f(\mathbf{p}) \phi_0 \quad (9a)$$

at leading order, where we have defined

$$\mathbf{p} = (p, q) = \nabla_{\boldsymbol{\xi}} g(\boldsymbol{\xi}) \quad \text{and} \quad f(\mathbf{p}) = \boldsymbol{\xi} \cdot \nabla_{\boldsymbol{\xi}} g(\boldsymbol{\xi}) - g(\boldsymbol{\xi}). \quad (9b)$$

The associated boundary conditions are deduced from (7b) as

$$\mathbf{n} \cdot (\nabla \phi_0 - \mathbf{p} \phi_0) = 0 \quad \text{on } \mathcal{B}. \quad (9c)$$

Eqs. (9), together with the periodicity (6) of ϕ_0 , define a family of eigenvalue problems parameterised by $\mathbf{p} = (p, q)$, which determine a discrete spectrum of eigenvalues $f(\mathbf{p})$. The eigenfunctions can be thought as functions $\phi_0(\mathbf{x}, \mathbf{p})$, using the one-to-one correspondence between $\boldsymbol{\xi}$ and \mathbf{p} . The eigenvalue problems can alternatively be rewritten in terms of

$$\psi = e^{-\mathbf{p} \cdot \mathbf{x}} \phi_0 \quad (10)$$

as the modified Helmholtz problems

$$\nabla^2 \psi = f(\mathbf{p})\psi, \quad \mathbf{n} \cdot \nabla \psi = 0 \quad \text{on } \mathcal{B}, \quad \psi(\mathbf{x} + \mathbf{r}_{n,m}, \mathbf{p}) = e^{-\mathbf{p} \cdot \mathbf{r}_{n,m}} \psi(\mathbf{x}, \mathbf{p}), \quad (11)$$

involving Neumann conditions on the obstacle boundaries and a ‘tilted’ periodicity condition.

We focus on the principal eigenvalue $f(\mathbf{p})$ of (9) or (11), that is, the eigenvalue with maximum real part, with associated eigenfunction $\phi_0(\mathbf{x}, \mathbf{p})$ (unique up to multiplication). The Krein–Rutman theorem implies that this eigenvalue is unique, simple and real. Moreover, $f \geq 0$ and convex. The rate function g is then deduced from f by Legendre transform since (9b) together with convexity implies that $f(\mathbf{p})$ and $g(\boldsymbol{\xi})$ are Legendre duals. Thus solving the family of eigenvalues problems (9) or (11) provide all the elements of the large-deviation approximation (5) of the scalar concentration.

For small $|\boldsymbol{\xi}|$, the rate function can be approximated as

$$g(\boldsymbol{\xi}) \sim \frac{1}{2} \boldsymbol{\xi}^T \nabla_{\boldsymbol{\xi}} \nabla_{\boldsymbol{\xi}} g(\mathbf{0}) \boldsymbol{\xi} = \frac{1}{4} \kappa_{\text{eff}}^{-1} |\boldsymbol{\xi}|^2, \quad |\boldsymbol{\xi}| \ll 1, \quad (12)$$

since the Hessian of g at $\mathbf{0}$ is isotropic (assuming a four-fold symmetry for (9)). Introducing this quadratic approximation into (5) recovers the diffusive approximation for θ obtained via homogenisation of the diffusion equation (1).

The eigenvalue problem (9) or (11) cannot be solved analytically, even for simple obstacle shapes. A useful lower bound can however be obtained: multiplying (9a) by ϕ_0 , integrating by parts over an elementary cell ω , and using the boundary and periodicity conditions gives

$$f(\mathbf{p}) \leq |\mathbf{p}|^2 \quad \text{and} \quad g(\boldsymbol{\xi}) \geq \frac{1}{4} |\boldsymbol{\xi}|^2 \quad (13)$$

with the second inequality obtained by taking a Legendre transform. Thus the presence of obstacles hinders dispersion [5, Th. 1.3] (note that f and therefore g may not vary monotonically with respect to the size of the obstacles [5, Th. 1.4]).

We note that, owing to the close connection between large deviations and chemical-front propagation in the Fisher–Kolmogorov–Petrovsky–Piskunov (FKPP) model [e.g. 8], the principal eigenvalue of (9) or (11) also determines the speed of these fronts [5], so that our results below also apply to this problem.

3 Circular obstacles in square lattices

We now focus on the simple geometry of Fig. 1, with circular obstacles of radius a arranged in square lattices with sides 2π , so that

$$\mathbf{r}_{m,n} = 2\pi(m, n), \quad (14)$$

and the obstacle area fraction is $\sigma = a^2/(4\pi)$. We solve the eigenvalue problem (9) numerically using a weak formulation described in Appendix B. We then use a standard finite-element discretisation: the eigenfunctions are approximated by continuous piecewise linear

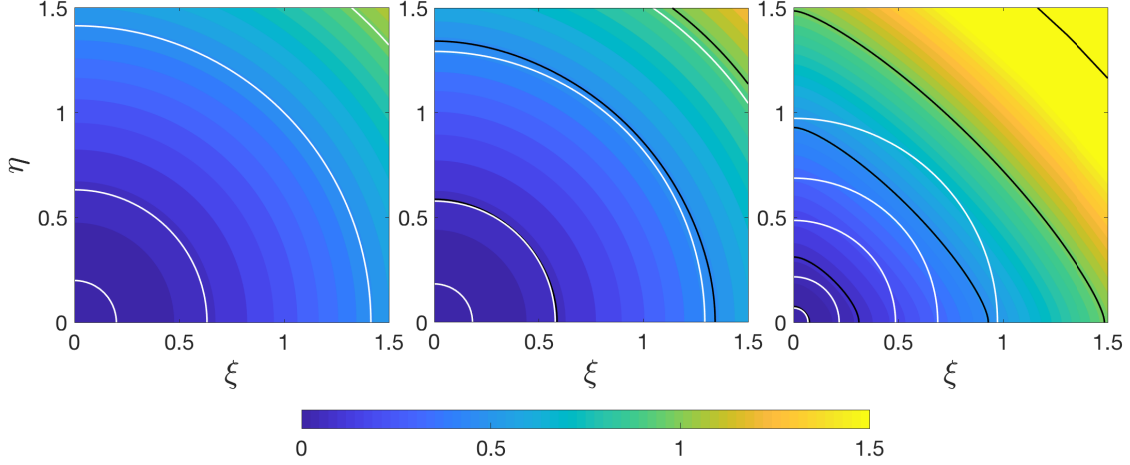


Figure 2: Rate function g plotted as a function of ξ for square lattices of circular obstacles with radius (left) $a = 0.01$, (middle) $\pi/2$ and (right) $\pi - 0.01$ (gap half width $\varepsilon = 0.01$). Selected contours (with values 0.01, 0.1, 0.5, 1 and 2) compare g (black) with its quadratic, Gaussian approximation (white) with the effective diffusivity κ_{eff} given by the Maxwell formula (3) (left), a best-fit estimate (middle) and the Keller formula (4) (right).

polynomials defined on a quasi-uniform triangular subdivision of the domain (obtained using Matlabs PDE Toolbox). This results in a large, sparse generalised matrix eigenvalue problem that we solve using the Shift-and-Invert method [18] to obtain an approximation for f on a grid of values of \mathbf{p} . Taking a numerical Legendre transform yields an approximation for g as a function of ξ . We now describe the results.

Figure 2 shows the rate function obtained for three obstacle radii $a = 0.01, \pi/2$ and $\pi - 0.01$ for ξ in the first quadrant (the other three quadrants are symmetric). The value $a = 0.01$ is representative of the dilute limit $a \ll 1$, the value $a = \pi - 0.01$ of the dense limit $\pi - a \ll 1$ with the area fraction close to the maximum $\sigma = \pi/4$ allowed by the lattice arrangement. The figure illustrates interesting features, such as anisotropy, which is absent for small obstacles (Fig. 2(a)) but very marked for the largest obstacles (Fig. 2(c)). As expected, the quadratic approximation (12) of $g(\xi)$ with effective diffusivity given by the Maxwell formula (3) in the dilute limit (Fig. 2(a)) or the Keller formula (4) in the dense limit (Fig. 2(b)) is accurate near $\xi = \mathbf{0}$. In the intermediate case, the quadratic behaviour also holds near $\xi = \mathbf{0}$ with an effective diffusivity that can be inferred from our results by contour fitting as an alternative to solving the cell problem of discretisation theory [16]. Remarkably, in the dilute case, the quadratic approximation is excellent beyond the small- ξ neighbourhood and applies to the entire range of ξ shown. In general and most strikingly in the dense case, g is a more complicated function of ξ for $|\xi| = O(1)$.

The physical implications of the above results are that homogenisation and the corresponding quadratic approximation (12) underestimate passive scalar transport. The phenomenon is most dramatic in the dense limit but negligible in the dilute limit. This is illus-

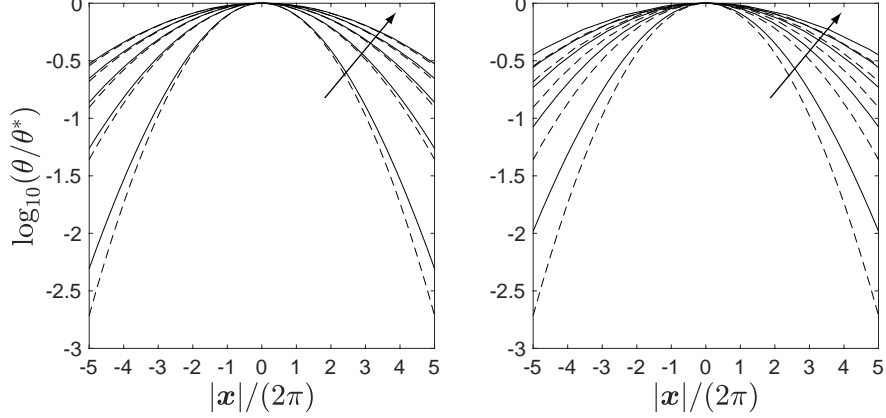


Figure 3: Normalised concentration $\theta(\mathbf{x}, t)/\theta^*$ (in logarithmic scale) where $\theta^* = \max_{\mathbf{x}} \theta(\mathbf{x}, t)$ plotted against $|\mathbf{x}|/(2\pi)$ for \mathbf{x} in the direction $(1, 1)$ at dimensionless times $\kappa_{\text{eff}}t/(4\pi^2) = 1, 2, 3, 4$ and 5 , with the arrow pointing in the direction of increasing t , for obstacles of radius $a = \pi - 0.01$ (left) and $\pi - 0.001$ (right) (corresponding to gap half width $\varepsilon = 0.01$ and 0.001). Numerical results (solid lines) obtained by solving (9) are compared with the Gaussian approximation with effective diffusivity κ_{eff} given by the Keller formula (4) (dashed lines).

trated in Figure 3 which focusses on two dense-limit cases: $a = \pi - 0.01$ and $\pi - 0.001$. It shows the (normalised) concentration $\theta(\mathbf{x}, t)$ in logarithmic scale along the diagonal $\mathbf{x} = |\mathbf{x}|(1, 1)/\sqrt{2}$ obtained at five consecutive times multiple of $4\pi^2/\kappa_{\text{eff}}$. This choice ensures that the time is sufficiently long for the large-deviation approximation (5) to apply. The figure compares the concentration obtained from the large-deviation approximation with its Gaussian, diffusive approximation (12) obtained with effective diffusivity given by the Keller formula (4). Clearly the discrepancy between the large-deviation approximation and its Gaussian, diffusive approximation is largest at early times, in the tails of $\theta(\mathbf{x}, t)$ and for the largest of the two radii. As time increases, the Gaussian, diffusive approximation describes the bulk of the scalar concentration increasingly better.

We can explain the validity of quadratic approximation (12) with effective diffusivity κ_{eff} given by the Maxwell formula (3) throughout the range of $\boldsymbol{\xi}$ by solving the eigenvalue problem (11) asymptotically in the dilute limit. This is carried out in Appendix A which shows that

$$f(\mathbf{p}) \sim (1 - \sigma) |\mathbf{p}|^2 \quad \text{and} \quad g(\boldsymbol{\xi}) \sim \frac{1}{4} (1 - \sigma)^{-1} |\boldsymbol{\xi}|^2 \quad (15)$$

for $\sigma = a^2/4\pi \ll 1$ and $|\mathbf{p}| = O(1)$. Thus, to leading order, the large-deviation approximation reproduces the results of classical homogenisation. In other words, the tails as well as the core of the distribution are Gaussian.

In the remainder of the paper we focus on the dense limit where the (i) limitations of the diffusive approximation, (ii) non-Gaussianity and (iii) anisotropic behaviour are most prominent. We use the gap half width $\varepsilon = \pi - a \ll 1$ as small parameter for an asymptotic

treatment.

4 Dense limit

4.1 Discrete network approximation

An intuitive way to understand the dense limit is to consider a discrete network model as a simplified analogue to the continuum model (1). The building block of this model is Keller's asymptotic solution leading to (4) [13]. This relies on the observation that the scalar concentration $\theta(\mathbf{x}, t)$ is nearly constant away from the small gaps separating neighbouring obstacles and changes rapidly along the gaps. The scalar flux is then localised in the gaps, unidirectional and approximately uniform in the direction transverse to the gaps. For a gap in the x -direction, for example, the total scalar flux is given by

$$F = 2h_\varepsilon(x) \frac{\partial \theta}{\partial x}, \quad (16)$$

where $h_\varepsilon(x)$ denotes the gap half width. For ε small, $h_\varepsilon(x)$ can be approximated as a parabola centred in the middle of the gap: $h_\varepsilon(x) \approx x^2/(2\pi) + \varepsilon$. Dividing across by $2h_\varepsilon(x)$, integrating and extending the integration range to $x \in (-\infty, \infty)$ gives the relationship

$$F = \alpha \Delta \theta, \quad \text{where } \alpha = \sqrt{2\varepsilon/\pi^3}, \quad (17)$$

between the total scalar flux and the difference $\Delta \theta$ in concentration between the two sides of the gap. This makes it possible to approximate (1) by a discrete network in which regions away from the gaps are represented as vertices and the gaps between them as edges. The (near-uniform) concentration $\theta_{m,n}$ inside the region centred at $\pi(2m+1, 2n-1)$ then evolves in response to the sum of the fluxes in adjacent gaps, leading to

$$\mathcal{A} \frac{d\theta_{m,n}}{dt} = \alpha(\theta_{m+1,n} + \theta_{m,n+1} + \theta_{m-1,n} + \theta_{m,n-1} - 4\theta_{m,n}), \quad (18)$$

where $\mathcal{A} = \pi^2(4-\pi)$ is the approximate area of the region. A rigorous justification of model (18) can be obtained using the techniques in [6].

It is easy to determine the long-time behaviour of (18). The diffusion approximation is recovered by taking the continuum limit of (18), approximating the right-hand side by $4\pi^2\alpha\nabla^2\theta$ to obtain the effective diffusivity

$$\kappa_{\text{eff}} = 4\pi^2\alpha/\mathcal{A} = \alpha/(1-\pi/4) \quad (19)$$

which is readily shown to match Keller's expression (4) using that $\sigma = \pi/4 - \varepsilon/2 + O(\varepsilon^2)$. However, the diffusive approximation is limited. Further information can be obtained from the rate function which appears in the large-deviation approximation $\theta_{m,n} \sim t^{-1} \exp(-tg_d(\mathbf{r}_{m,n}/t))$ of solutions of the network model (18). Substituting into (18) gives an explicit relation for the Legendre transform $f_d(\mathbf{p})$ of $g_d(\boldsymbol{\xi})$, namely

$$f_d(\mathbf{p}) = \frac{4\alpha}{\mathcal{A}} \left(\sinh^2(\pi p) + \sinh^2(\pi q) \right). \quad (20)$$

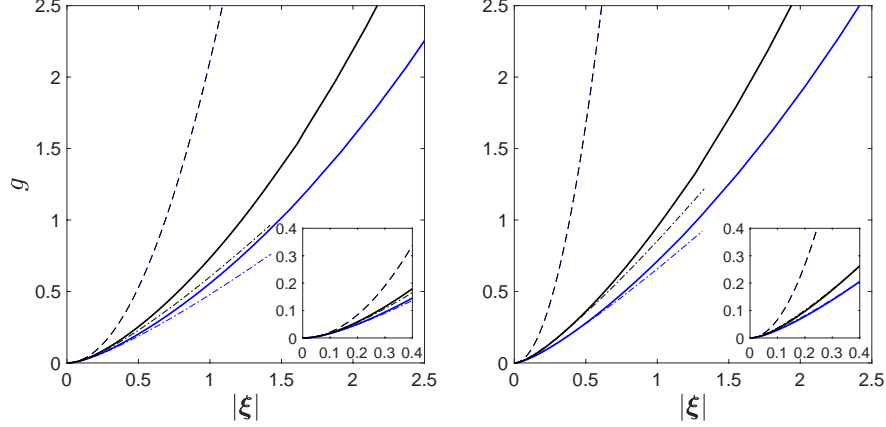


Figure 4: Rate function g plotted against $|\xi|$ for obstacles of radius (left) $a = \pi - 0.01$ and (right) $\pi - 0.001$ (corresponding to gap half width $\varepsilon = 0.01$ and 0.001) in the directions $(1, 1)$ (black) and $(1, 0)$ (blue). Numerical results (thick solid lines) obtained by solving (9) are compared to the quadratic approximation (12) (dashed lines) and the network approximation (21) (dashed-dotted). The insets focus on small values of $|\xi|$.

Taking the Legendre transform of (20) then yields

$$g_d(\xi) = \frac{2\alpha}{\mathcal{A}} (S(\beta\xi) + S(\beta\eta)), \quad (21)$$

where $S(x) = 1 + x \sinh^{-1} x - \sqrt{1 + x^2}$ and $\beta = \mathcal{A}/(4\pi\alpha)$. Figure 4 shows that the rate function (21) is an improvement to the quadratic (Gaussian) approximation. Nevertheless this improvement is limited to small values of $|\xi|$. This is because a key assumption of the network model, namely that the concentration is nearly uniform outside the gaps, breaks down for $|\mathbf{x}|$ large enough that $|\xi|$ is not small. We now carry out an asymptotic analysis that yields an approximation to rate function that is valid for $|\xi| = O(1)$ and recovers (21) as a limiting case.

4.2 Asymptotics

We apply matched asymptotics to obtain an approximation to the solution of the eigenvalue problem (11) for $\varepsilon \ll 1$ that is valid in the distinguished regime $|\mathbf{p}| = O(1)$. The analysis is conveniently carried out in the translated elementary cell ω' shown in Fig. 1. This is centred on the star-like region which we will (inaccurately) refer to as ‘astroid’ in the limit $\varepsilon \rightarrow 0$, when the gaps close to form four cusps.

We first consider the solution inside a representative gap, to the west of the centre. The gap boundaries are given by

$$y = -\pi \pm h_\varepsilon(x), \quad \text{where} \quad h_\varepsilon(x) = \pi - ((\pi - \varepsilon)^2 - x^2)^{1/2}, \quad 0 \leq x \leq \pi - \varepsilon. \quad (22)$$

This form suggests an *outer region* where $x, y + \pi = O(1)$ in which case (22) may be approximated as the boundary of the astroid,

$$y = -\pi \pm h_0(x) + O(\varepsilon) \quad \text{where} \quad h_0(x) = \pi - \sqrt{\pi^2 - x^2}, \quad 0 \leq x \leq \pi, \quad (23)$$

and an *inner region* where $X = x/\sqrt{\varepsilon} = O(1)$ and $Y = (y + \pi)/\varepsilon = O(1)$ in terms of which (22) is approximately given by

$$Y = \pm H_\varepsilon(X) = \pm H_0(X) + O(\varepsilon) \quad \text{where} \quad H_0(X) = \frac{X^2}{2\pi} + 1. \quad (24)$$

4.2.1 Inner region

Inside the inner region, the modified Helmholtz problem (11) becomes

$$\varepsilon \partial_{XX} \Psi + \partial_{YY} \Psi = \varepsilon^2 f \Psi. \quad (25a)$$

for the eigenfunction $\Psi(X, Y) = \psi(x, y)$, with the Neumann boundary condition approximated by

$$\pm \partial_Y \Psi - \varepsilon \left(\frac{X}{\pi} \partial_X \Psi \pm \frac{X^2}{2\pi^2} \partial_Y \Psi \right) + O(\varepsilon^{3/2}) = 0 \quad \text{at} \quad Y = \pm H_0(X) + O(\varepsilon). \quad (25b)$$

We now introduce the expansions

$$\Psi = \Psi_0 + \varepsilon^{1/2} \Psi_1 + \varepsilon \Psi_2 + O(\varepsilon^{3/2}) \quad \text{and} \quad f = f_0 + \varepsilon^{1/2} f_1 + \varepsilon f_2 + O(\varepsilon^{3/2}). \quad (26)$$

of the eigenvalue and eigenfunction into (25) to obtain, at $O(1)$ and $O(\varepsilon^{1/2})$,

$$\partial_{YY} \Psi_i = 0 \quad \text{with} \quad \partial_Y \Psi_i = 0 \quad \text{at} \quad Y = \pm H_0(X) \quad (i = 0, 1) \quad (27)$$

and thus $\Psi_0 = \Psi_0(X)$ and $\Psi_1 = \Psi_1(X)$ i.e., they are transversely uniform. The key equation appears at $O(\varepsilon)$. Using the Y -independence of Ψ_0 it simplifies to

$$\partial_{YY} \Psi_2 = -\partial_{XX} \Psi_0 \quad \text{with} \quad \mp \partial_Y \Psi_2 = \frac{1}{\pi} X \partial_X \Psi_0 \quad \text{at} \quad Y = \pm H_0(X). \quad (28)$$

Integrating (28) for $Y \in [-H_0(X), H_0(X)]$ we find that $\partial_X(H_0(X) \partial_X \Psi_0) = 0$, hence

$$\Psi_0 = A_1 \int_0^X \frac{dX'}{h(X')} + B_1 = \sqrt{2\pi} A_1 \tan^{-1} \left(\frac{X}{\sqrt{2\pi}} \right) + B_1, \quad X = x/\varepsilon^{1/2}. \quad (29a)$$

for constants A_1 and B_1 to be determined by matching with the outer solution. Similarly, using symmetry, the solution inside the gaps to the south, east and north of the centre are

$$\Psi_0 = A_2 \sqrt{2\pi} \tan^{-1} \left(\frac{Y}{\sqrt{2\pi}} \right) + B_2, \quad Y = (y + 2\pi)/\varepsilon^{1/2}, \quad (29b)$$

$$\Psi_0 = A_3 \sqrt{2\pi} \tan^{-1} \left(\frac{X}{\sqrt{2\pi}} \right) + B_3, \quad X = (x - 2\pi)/\varepsilon^{1/2}, \quad (29c)$$

$$\Psi_0 = A_4 \sqrt{2\pi} \tan^{-1} \left(\frac{Y}{\sqrt{2\pi}} \right) + B_4, \quad Y = y/\varepsilon^{1/2}, \quad (29d)$$

introducing additional constants A_i and B_i for $i = 2, 3, 4$. The constants are constrained by the ‘tilted’ periodicity condition (11), giving

$$(A_3, B_3) = e^{-2\pi p}(A_1, B_1) \quad \text{and} \quad (A_4, B_4) = e^{-2\pi q}(A_2, B_2). \quad (30)$$

4.2.2 Outer region and matching

In the outer region we assume the expansion

$$\psi = \psi_0 + \varepsilon^{1/2}\psi_1 + \varepsilon\psi_2 + O(\varepsilon^{3/2}). \quad (31)$$

To leading-order ψ_0 satisfies

$$\nabla^2\psi_0 = f_0\psi_0, \quad \mathbf{n} \cdot \nabla\psi_0 = 0 \quad \text{on} \quad y = -\pi \pm \begin{cases} h_0(x) & \text{for } 0 \leq x < \pi \\ h_0(2\pi - x) & \text{for } \pi \leq x < 2\pi \end{cases}. \quad (32a)$$

Additional boundary conditions are obtained by matching the solution near the cusps of the astroid with the inner solutions (29). Near the cusp to the west of the centre, ψ_0 satisfies the approximation $\partial_x(h_0(x)\partial_x\psi_0) = 0$ to (32a) (obtained following similar steps as in §4.2.1), hence

$$x^2\partial_x\psi_0 \sim C_1, \quad \text{as } \mathbf{x} \rightarrow \mathbf{x}_1 = (0, -\pi), \quad (32b)$$

where C_1 is a constant to be determined. The behaviour is similar near the other three cusps located at $\mathbf{x}_2 = (\pi, -2\pi)$, $\mathbf{x}_3 = (2\pi, -\pi)$ and $\mathbf{x}_4 = (\pi, 0)$ involving constants C_i for $i = 2, 3, 4$.

Canonical boundary-value problem. Exploiting the four-fold symmetry the solution to (32) can be written as the linear combination

$$\psi_0(x, y) = C_1\psi^*(x, y) + C_2\psi^*(y + 2\pi, -x) + C_3\psi^*(2\pi - x, -y - 2\pi) + C_4\psi^*(-y, x) \quad (33)$$

of the solution ψ^* of the canonical boundary-value problem

$$\nabla^2\psi^* = f_0\psi^*, \quad (34a)$$

with Neumann boundary conditions on the astroid except on the western cusp where

$$x^2\partial_x\psi^* \rightarrow 1 \quad \text{as } \mathbf{x} \rightarrow \mathbf{x}_1. \quad (34b)$$

The key point is that solving (34) serves to determine four functions $D_i(f_0)$, ($i = 1, \dots, 4$) defined by

$$\psi^* \sim -\frac{1}{x} - D_1(f_0) \quad \text{as } \mathbf{x} \rightarrow \mathbf{x}_1 \quad \text{and} \quad \psi^* \sim -D_i(f_0) \quad \text{as } \mathbf{x} \rightarrow \mathbf{x}_i \quad \text{for } i = 2, 3, 4. \quad (35)$$

Thus, these functions describe the leading-order behaviour of ψ^* once the singular contribution $-1/x$ at \mathbf{x}_1 is subtracted out. By symmetry

$$D_4(f_0) = D_2(f_0). \quad (36)$$

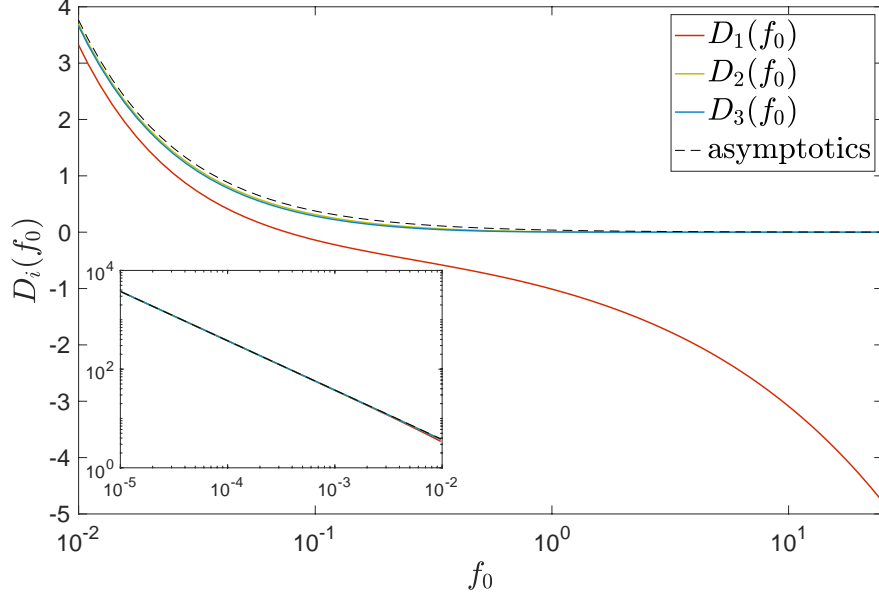


Figure 5: Functions D_i ($i = 1, 2, 3$) defined by (35) against f_0 . The numerical estimates (solid lines) are compared with the asymptotic approximation (40) for $f_0 \ll 1$ (dashed line).

We obtain the functions $D_i(f_0)$ by solving (34) numerically for a range of values of f_0 using a standard finite-element discretisation. The difficulty associated with the singular shape of the astroid is avoided by trimming off the cusp regions with four straight segments placed a small distance δ away from each cusp. Fig. 5 shows the results obtained for a range of values of f_0 . These results have been checked to be insensitive to the value of δ as well as to the resolution of the finite-element discretisation ($\delta = 0.01$ for the figure). Fig. 6 shows the form of ψ^* for different values of f_0 . Clearly, larger values of f_0 , corresponding to larger values of \mathbf{p} , lead to higher contrasts in ψ_0 , reflecting the fact that the asymptotic analysis goes beyond the hypothesis of near-uniform concentration assumed for the discrete network approximation of §4.1.

The asymptotic behaviour of $D_i(f_0)$ for small f_0 is useful for later reference. In this limit, the solution ψ^* may be expanded according to

$$\psi^* = f_0^{-1}\psi_0^* + \psi_1^* + O(f_0), \quad f_0 \ll 1. \quad (37)$$

Substituting (37) into (34a), we obtain that

$$\nabla^2 \psi_0^* = 0 \quad \text{and} \quad \nabla^2 \psi_1^* = \psi_0^*. \quad (38a)$$

Additionally, from (34b) we have that ψ_0^* and ψ_1^* satisfy Neumann boundary conditions on the astroid except on the western cusp where ψ_1^* satisfies

$$x^2 \partial_x \psi_1^* \rightarrow 1 \quad \text{as } \mathbf{x} \rightarrow \mathbf{x}_1. \quad (38b)$$

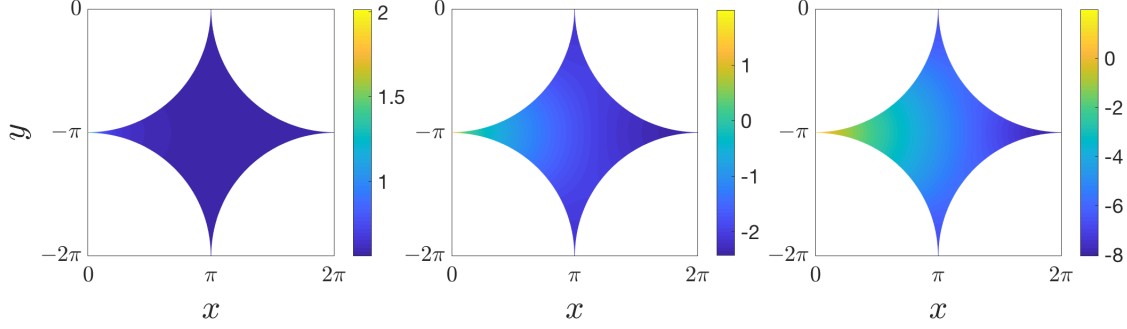


Figure 6: Logarithm $\log_{10} |\psi^*|$ of $\psi^*(\mathbf{x})$ defined as the solution to the canonical boundary-value problem (34) obtained for (left) $f_0 = 0.01$, (middle) 1 and (right) 10.

Thus, $\psi_0^* = c$ where c is a constant. The value of c may be determined by integrating the second equation in (38a) and using (38b) to obtain

$$\mathcal{A}c = \int_{\omega'} \nabla^2 \psi_1^* d\mathbf{x} \sim -\lim_{\delta \rightarrow 0} \int_{-\delta^2/(2\pi)}^{\delta^2/(2\pi)} \partial_x \psi_1^*|_{x=\delta} dy = -\frac{1}{\pi}, \quad (39)$$

with the area \mathcal{A} defined in (18). Therefore

$$D_i(f_0) \sim \frac{1}{\pi \mathcal{A} f_0} \quad \text{for } f_0 \ll 1 \quad (i = 1, \dots, 4). \quad (40)$$

Figure 5 confirms the validity of (40).

Matching. The leading-order approximation to the eigenvalue $f(\mathbf{p})$ is obtained by matching the solution in the inner and outer regions. Comparing (29) with (33) using (35) and (36) leads to

$$C_1 = -2\pi\sqrt{\varepsilon}A_1, \quad -C_1D_1(f_0) - (C_2 + C_4)D_2(f_0) - C_3D_3(f_0) = \sqrt{\pi^3/2}A_1 + B_1, \quad (41a)$$

$$C_2 = -2\pi\sqrt{\varepsilon}A_2, \quad -(C_1 + C_3)D_2(f_0) - C_2D_1(f_0) - C_3D_4(f_0) = \sqrt{\pi^3/2}A_2 + B_2, \quad (41b)$$

$$C_3 = 2\pi\sqrt{\varepsilon}A_3, \quad -C_1D_3(f_0) - (C_2 + C_4)D_2(f_0) - C_3D_1(f_0) = -\sqrt{\pi^3/2}A_3 + B_3, \quad (41c)$$

$$C_4 = 2\pi\sqrt{\varepsilon}A_4, \quad -(C_1 + C_3)D_2(f_0) - C_2D_3(f_0) - C_4D_1(f_0) = -\sqrt{\pi^3/2}A_4 + B_4. \quad (41d)$$

We now use (30) to reduce (41) to a homogeneous linear system for two of the constants, e.g., A_1 and A_2 . Non-trivial solutions exist provided that the determinant of the associated matrix vanish. After some manipulations using (36) this gives

$$\begin{aligned} & (D_3(f) \cosh(2\pi p) - D_1(f) - (2\pi\alpha)^{-1}) (D_3(f) \cosh(2\pi q) - D_1(f) - (2\pi\alpha)^{-1}) \\ & - D_2^2(f) (\cosh(2\pi p) - 1) (\cosh(2\pi q) - 1) = 0 \end{aligned} \quad (42)$$

with $\alpha = \sqrt{2\varepsilon/\pi^3}$ as defined in (17) and we omit the subscript of f_0 .

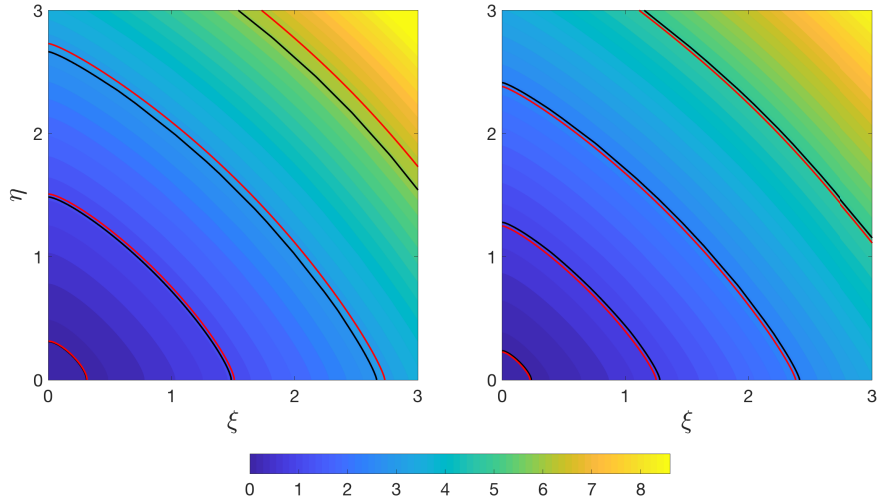


Figure 7: Rate function g plotted against $|\boldsymbol{\xi}|$ for square lattice of circular obstacles with radius $a = \pi - 0.01$ (left) and $\pi - 0.001$ (right) (corresponding to gap half widths $\varepsilon = 0.01$ and 0.001) obtained by solving the eigenvalue problem (9). Selected contours (with values 0.1, 1, 2.5 and 5) compare the numerical g (black) with the asymptotic approximation deduced from (42) (red).

Eq. (42) is the central result of this paper. It is a transcendental equation for the Legendre transform f of the rate function g as a function of the gap half width ε . Once the functions $D_i(f)$ have been tabulated, it reduces the determination f and hence g to an algebraic problem. The transcendental dependence of f on ε reflects the uniform validity of our approximation across a range of values of \boldsymbol{p} , including in particular a regime where $\sqrt{\varepsilon}e^{2\pi|\boldsymbol{p}|} = O(1)$ as well as the discrete network regime of §4.1.

We solve (42) numerically for a range of \boldsymbol{p} to obtain $f(\boldsymbol{p})$ and $g(\boldsymbol{\xi})$ by Legendre transform. In practice, it is convenient to express \boldsymbol{p} in polar form and, for fixed angle φ , solve for $|\boldsymbol{p}|$ as a function of f using a nonlinear solver such as Matlab's `fzero`. The computation needs a good first guess which we obtain by noting that, when $\varphi = 0$, i.e. for $\boldsymbol{p} = |\boldsymbol{p}|(1, 0)$, (42) reduces to $|\boldsymbol{p}| = 1/(2\pi) \cosh^{-1}((D_1(f) + \alpha^{-1})/D_3(f))$. We then iterate over increasing values of φ using the value of $|\boldsymbol{p}|$ determined previously as an initial guess for the next solution.

Fig. 7 compares the asymptotic prediction for $g(\boldsymbol{\xi})$ deduced from (42) to that obtained by finite-element solution of the full eigenvalue problem (9) for $\varepsilon = 0.01$ and 0.001 . The agreement is excellent throughout the range of $|\boldsymbol{\xi}|$, showing that our approximation captures the scalar concentration deep into the tails. This is more clearly demonstrated in Fig. 8 which displays cross-sections of $g(\boldsymbol{\xi})$ for $\boldsymbol{\xi}$ along the ξ -axis and along the diagonal $\xi = \eta$ and for a very wide range of values of $|\boldsymbol{\xi}|$. While some discrepancies between asymptotic and numerical solutions are visible for $\varepsilon = 0.01$ the solutions match perfectly for $\varepsilon = 0.001$.

For very large $|\boldsymbol{\xi}|$, the concentrations are exceedingly small, of course. It is nonetheless interesting to note that $g(\boldsymbol{\xi})$ is then controlled by an action-minimising trajectory as predicted by the Friedlin–Wentzell (small-noise) large-deviation theory [9]. This gives the asymptotics

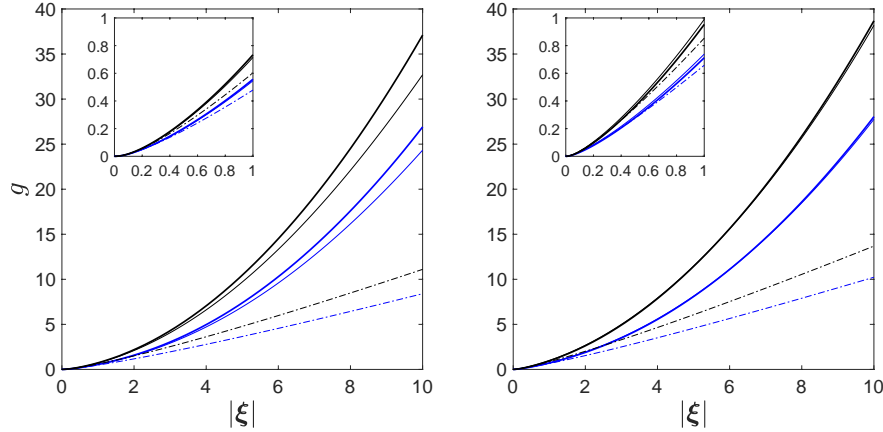


Figure 8: Cross-section of the rate function g in Fig. 7 in the directions $(1, 1)$ (black lines) and $(1, 0)$ (lines). Numerical results obtained by solving (9) (thick solid lines) are compared against the asymptotic approximation derived from (42) (thin solid lines) and from the discrete-network approximation (20) (dashed-dotted). The insets focus on small values of $|\xi|$.

$g(\xi) \sim d^2(\xi)/4$ and hence $\theta \propto e^{-d^2(\mathbf{x}-\mathbf{x}_0)/(4t)}$ where $d(\mathbf{x}) = \pi(x+y)/4 + (1-\pi/4)|x-y|$ is the distance along the shortest path (made up of quarter circles and a line segment (horizontal if $x > y$, vertical if $x < y$) joining \mathbf{x}_0 to \mathbf{x} while avoiding the obstacles. Thus, at very large distances, one recovers a diffusive behaviour with the molecular value of the diffusivity but a non-Euclidean distance determined by the obstacle geometry (see [22] for a similar phenomenon in a different geometry).

We conclude by checking explicitly that our asymptotic analysis recovers the discrete network approximation (20). This approximation arises from the transcendental equation (42) in the limit of small f : introducing the small- f asymptotic approximation (40) of the D_i into (42) gives

$$\begin{aligned} & (\cosh(2\pi p) - 1 - \mathcal{A}f/(2\alpha)) (\cosh(2\pi q) - 1 - \mathcal{A}f/(2\alpha)) \\ & - (\cosh(2\pi p) - 1) (\cosh(2\pi q) - 1) = 0, \end{aligned} \quad (43)$$

which simplifies as $f = f_d$ with the network expression (20) of f_d . The corresponding rate function g_d is compared with the asymptotic and numerical estimates of g in Fig. 8 which demonstrates the superiority of our asymptotic result over the network approximation.

5 Conclusions

This paper revisits the classical results of Maxwell, Rayleigh, Keller and many others since on the impact of an array of obstacles on the diffusion of scalars in an otherwise homogeneous medium. Homogenisation theory predicts that, at a coarse-grained level, a scalar released

instantaneously simply diffuses with a (computable) effective diffusivity. A basic observation is that this conclusion is restricted to the bulk of the scalar distribution and that the more general tool of large-deviation theory is necessary to capture the tails of the distribution. Focusing on the case of a square lattice of circular obstacles for simplicity, we show that the non-diffusive behaviour is leading to tail concentrations that are much fatter than predicted by the effective diffusion approximation. This effect is strongest in the dense limit, when the obstacles are nearly touching and large-scale dispersion is strongly inhibited. We examine this limit using a matched-asymptotics approach which reduces the computation of the large-deviation rate function – requiring in general the solution of a family of elliptic eigenvalue problems – to the algebraic equation (42). The rate function that is obtained in this way captures the scalar concentration over a wide range of distances from the point of release and encompasses several physical regimes: the diffusive regime with Keller’s effective diffusivity [13], a closely related regime associated with a lattice random walk, all the way to the extreme-tail regime where the scalar concentration is controlled by single shortest-distance paths.

Our results exemplify a general phenomenon, relevant to a broad range of applications in porous media, composites and metamaterials, which takes its full significance when low concentrations are critical. This is the case in the presence of chemical reactions, as the example of the FKPP model makes plain. This adds the logistic term $\alpha\theta(1 - \theta)$, with α the reaction rate, to the right-hand side of the diffusion equation (1a). It leads to the propagation of fronts with speed $c(\mathbf{e})$ in the direction of the unit vector \mathbf{e} . This speed can be deduced from the rate function by solving $g(c(\mathbf{e})\mathbf{e}) = \alpha$ or equivalently from its Legendre transform as $c(\mathbf{e}) = \inf_{p>0} (f(p\mathbf{e}) + \alpha)/p$ [8, 21]. This provides an explicit example of a macroscopic manifestation of the tail behaviour of the scalar concentration.

We conclude by mentioning several directions in which our results could be extended. A first direction is to adapt our approach to consider different, more complex obstacle geometries, with extension from the square lattice to other Bravais lattices and from two to three dimensions, e.g. with spherical obstacles. A second direction would incorporate the effect of an incompressible flow by solving the appropriate family of eigenvalue problems. One expects that the interaction between the inhomogeneity in the flow and in the domain will lead to interesting dispersion regimes, dependent on the size of the obstacles and the intensity of the flow (see e.g. [15, 4] for the corresponding regimes obtained using homogenisation theory). A third direction concerns the nearly periodic case, introducing modulations in the arrangement and size of the obstacles over long spatial scales (see [7] for corresponding homogenisation results). A fourth direction is to examine random distributions of obstacles such as those considered in [12, 19]. The fifth and final direction we suggest is the transfer of the tools of large-deviation theory from the (parabolic) diffusion equation to the (hyperbolic) wave equation, with applications to acoustics and photonics. Results are available about the effective wave speed (the analogue of the effective diffusivity) in media with obstacles, including in the dense limit [23]; it would be desirable to extend these to capture wave propagation over very large distances and to apply large deviations to go beyond simple dispersive corrections to homogenisation [1].

Data accessibility. A MATLAB code to solve (9) numerically can be found at <https://bitbucket.org/loghind/eigfem-homogenisation/>.

Acknowledgments. A. Tzella and D. Loghin acknowledge A. Patel for his contribution to a related MSci project. Y. Farah acknowledges the support of a PhD scholarship from the UK Engineering and Physical Sciences Research Council.

A Dilute limit

We employ matched asymptotic expansions to approximate the solution to (9) for $a \ll 1$ in the distinguished regime $|\mathbf{p}| = O(1)$. This is straightforward to achieve by decomposing the elementary cell ω shown in Fig. 1 into an *outer region* where $r = |\mathbf{x}| = O(1)$, and an *inner region* where $R = |\mathbf{X}| = r/a = O(1)$, and by expanding

$$f \sim |\mathbf{p}|^2 + o(a), \quad \psi \sim \psi_0 + o(a) \quad \text{and} \quad \Psi \sim \Psi_0 + o(a) \quad \text{as } a \rightarrow 0, \quad (44)$$

for the eigenvalue and eigenfunction in the outer and inner regions respectively. Clearly, $\psi_0 = e^{-\mathbf{p} \cdot \mathbf{x}}$ is the leading-order solution to (11). Substituting the inner expansion inside (11), we find that Ψ_0 satisfies Laplace's equation

$$\frac{1}{R} \frac{\partial}{\partial R} \left(R \frac{\partial \Psi_0}{\partial R} \right) + \frac{1}{R^2} \frac{\partial^2 \Psi_0}{\partial \theta^2} = 0 \quad (45a)$$

in polar coordinates (R, θ) , with Neumann condition on the boundary of the obstacle

$$\frac{\partial \Psi_0}{\partial R} = 0 \quad \text{at} \quad R = 1. \quad (45b)$$

Let $\mathbf{p} = |\mathbf{p}|(\cos \varphi, \sin \varphi)$. The matching of Ψ_0 with ψ_0 is ensured provided that

$$\Psi_0 = 1 - a|\mathbf{p}|R \cos(\theta - \varphi) \quad \text{as } R \rightarrow \infty. \quad (45c)$$

The solution to (45) is then

$$\Psi_0 = 1 - a|\mathbf{p}|(R + R^{-1}) \cos(\theta - \varphi). \quad (46)$$

The leading-order inner and outer solutions may be used to obtain a higher-order correction to the eigenvalue $f(\mathbf{p})$. Multiplying (11) by $\exp(\mathbf{p} \cdot \mathbf{x})$ and integrating by parts over ω gives

$$\int_{\partial\omega} e^{\mathbf{p} \cdot \mathbf{x}} \mathbf{n} \cdot \nabla \psi \, dl + \int_{\partial\omega} e^{\mathbf{p} \cdot \mathbf{x}} \mathbf{n} \cdot \mathbf{p} \psi \, dl = (f - |\mathbf{p}|^2) \int_{\omega} e^{\mathbf{p} \cdot \mathbf{x}} \psi \, d\mathbf{x}. \quad (47)$$

We use the ‘tilted’ periodicity condition (11) to deduce that $\exp(\mathbf{p} \cdot \mathbf{x})\psi$ and $\exp(\mathbf{p} \cdot \mathbf{x})\nabla\psi$ are periodic and therefore contributions along opposing edges of the square boundary cancel. After applying the boundary condition (9c), we are left with

$$(f - |\mathbf{p}|^2) \int_{\omega} e^{\mathbf{p} \cdot \mathbf{x}} \psi \, d\mathbf{x} = \int_{\mathcal{C}_a} e^{\mathbf{p} \cdot \mathbf{x}} \mathbf{n} \cdot \mathbf{p} \psi \, dl \quad (48)$$

where \mathcal{C}_a denotes the circle of radius a centred at the origin. We use $\psi \sim \psi_0 = e^{-\mathbf{p} \cdot \mathbf{x}}$ to approximate the left-hand side of (48) and

$$\psi|_{r=a} = \Psi|_{R=1} \sim \Psi_0(1, \theta; a) = 1 - 2a|\mathbf{p}| \cos(\theta - \varphi) + o(a) \quad \text{and} \quad e^{\mathbf{p} \cdot \mathbf{x}} = 1 + a|\mathbf{p}| \cos(\theta - \varphi) + o(a) \quad (49)$$

to approximate the right-hand side of (48). Carrying out the integrations we obtain $f(\mathbf{p})$ and, after Legendre transform, $g(\boldsymbol{\xi})$ as the quadratic functions (15).

We note that the quadratic approximations (15) hold in the dilute limit for obstacles of arbitrary shapes, because only the far-field, dipolar form of the inner solution matters at leading order.

B Weak form of the eigenvalue problem (9)

A weak form of the eigenvalue problem (9) is readily obtained by considering φ to be a general function (square-integrable, including its derivatives) satisfying the same periodicity condition (6) as ϕ . Multiplying (9a) by φ and integrating by parts over the elementary cell ω gives

$$(f(\mathbf{p}) - |\mathbf{p}|^2) \int_{\omega} \phi \varphi d\mathbf{x} = \int_{\partial\omega} \mathbf{n} \cdot \nabla \phi \varphi ds - \int_{\omega} (\nabla \phi \cdot \nabla \varphi + 2\mathbf{p} \cdot \nabla \phi \varphi) d\mathbf{x}. \quad (50)$$

We use the periodicity condition (6) to deduce that contributions along opposing edges of the square boundary cancel. Upon application of the boundary condition (9c), equation (50) becomes

$$(f(\mathbf{p}) - |\mathbf{p}|^2) \int_{\omega} \phi \varphi d\mathbf{x} = - \int_{\omega} (\nabla \phi \cdot \nabla \varphi + \mathbf{p} \cdot (\nabla \varphi \phi - \nabla \phi \varphi)) d\mathbf{x}, \quad (51)$$

where we have used $\int_{\omega} \mathbf{p} \cdot \nabla \phi \varphi d\mathbf{x} = \int_{\mathcal{C}_a} \mathbf{p} \cdot \mathbf{n} \phi \varphi ds - \int_{\omega} \mathbf{p} \cdot \nabla \varphi \phi d\mathbf{x}$ to simplify. A standard Galerkin finite element projection of (51) onto the space of degree-one continuous piecewise-linear polynomials defined on a quasi-uniform triangular subdivision of ω yields a generalised eigenvalue problem that we solve numerically.

References

- [1] A. Abdulle and T. Pouchon. Effective models for long time wave propagation in locally periodic media. *SIAM J. Numer. Anal.*, 56:2701–2730, 2018.
- [2] G. Allaire, M. Briane, R. Brizzi, and Y. Capdeboscq. Two asymptotic models for arrays of underground waste containers. *Appl. Anal.*, 88(10-11):1445–1467, 2009.
- [3] B. Amaziane, S. N. Antontsev, L. Pankratov, and A. L. Piatnitski. Homogenization of immiscible compressible two-phase flow in porous media: Application to gas migration in a nuclear waste repository. *Multiscale Model. Simul.*, 8:2023–2047, 2010.

- [4] J. Auriault and P. Adler. Taylor dispersion in porous media: Analysis by multiple scale expansions. *Adv. Water Resour.*, 18:217–226, 1995.
- [5] H. Berestycki, F. Hamel, and N. Nadirashvili. The speed of propagation for KPP type problems. I: Periodic framework. *J. Eur. Math. Soc.*, 007(2):173–213, 2005.
- [6] L. Berlyand, A. Novikov, and K. Alexander. *Introduction to the Network Approximation Method for Materials Modeling*. Cambridge University Press, 2012.
- [7] M. Bruna and S. Chapman. Diffusion in spatially varying porous media. *SIAM J. Appl. Math.*, 75:16481674, 2015.
- [8] M. I. Freidlin. *Functional Integration and Partial Differential Equations*. Princeton University Press, 1985.
- [9] M. I. Freidlin and A. D. Wentzell. *Random perturbations of dynamical systems*. Springer, 1984.
- [10] P. H. Haynes and J. Vanneste. Dispersion in the large-deviation regime. Part I: shear flows and periodic flows. *J. Fluid Mech.*, 745:321–350, 2014.
- [11] U. Hornung, editor. *Homogenization and Porous Media*. Springer, 1997.
- [12] V. V. Jikov, S. M. Kozlov, and O. Oleinik. *Homogenization of Differential Operators and Integral Functionals*. Springer-Verlag, Berlin, 1994.
- [13] J. B. Keller. Conductivity of a medium containing a dense array of perfectly conducting spheres or cylinders or nonconducting cylinders. *J. Appl. Phys.*, 34(4):991–993, 1963.
- [14] J. C. Maxwell. *Treatise on Electricity and Magnetism*. Clarendon Press, Oxford, 1873.
- [15] C. C. Mei. Method of homogenisation applied to dispersion in porous media. *Transport Porous Med.*, 9(3):261–274, 1992.
- [16] W. T. Perrins, D. R. McKenzie, R. C. McPhedran, and R. Brown. Transport properties of regular arrays of cylinders. *Proc. R. Soc. London A*, 369:207–225, 1979.
- [17] J. W. Rayleigh. On the influence of obstacles arranged in rectangular order upon the properties of the medium. *Phil. Mag.*, 34(241):481–491, 1892.
- [18] Y. Saad. *Numerical methods for large eigenvalue problems*, volume 66 of *Classics in Applied Mathematics*. Society for Industrial and Applied Mathematics (SIAM), Philadelphia, PA, 2011. Revised edition of the 1992 original.
- [19] S. Torquato. *Random Heterogeneous Materials: Microstructure and Macroscopic Properties*. Springer, 2002.

- [20] H. Touchette. The large deviation approach to statistical mechanics. *Phys. Rep.*, 478(1–3):1–69, 2009.
- [21] A. Tzella and J. Vanneste. FKPP fronts in cellular flows: The Large-Péclet regime. *SIAM J. Appl. Math.*, 75(4):1789–1816, 2015.
- [22] A. Tzella and J. Vanneste. Dispersion in rectangular networks: Effective diffusivity and large-deviation rate function. *Phys. Rev. Lett.*, 117:114501, 2016.
- [23] A. L. Vanel, O. Schnitzer, and R. V. Craster. Asymptotic network models of sub-wavelength metamaterials formed by closely packed photonic and phononic crystals. *Europhys. Lett.*, 119(6):64002, 2017.